# Figuring Out Gas & Galaxies In Enzo (FOGGIE). XIII. On the Observability of Extended H I Disks and Warps

Cameron W. Trapp  $^{\bullet}$ , Molly S. Peeples  $^{\bullet}$ , Jason Tumlinson  $^{\bullet}$ , Brian W. O'Shea  $^{\bullet}$ , Shea  $^{\bullet}$ , Anna C. Wright  $^{\bullet}$ , Ayan Acharyya  $^{\bullet}$ , Britton D. Smith  $^{\bullet}$ , Vida Saeedzadeh  $^{\bullet}$ , and Ramona Augustin  $^{\bullet}$ 100

<sup>1</sup> Center for Astrophysical Sciences, William H. Miller III Department of Physics & Astronomy, Johns Hopkins University, 3400 N.
Charles Street, Baltimore, MD 21218

<sup>2</sup> Space Telescope Science Institute, 3700 San Martin Dr., Baltimore, MD 21218
 <sup>3</sup> Department of Computational Mathematics, Science, and Engineering, Michigan State University, East Lansing, MI, US
 <sup>4</sup> Department of Physics and Astronomy, Michigan State University, East Lansing, MI, US
 <sup>5</sup> Facility for Rare Isotope Beams, Michigan State University, East Lansing, MI 48824, USA
 <sup>6</sup> Institute for Cyber-Enabled Research, 567 Wilson Road, Michigan State University, East Lansing, MI 48824
 <sup>7</sup> Center for Computational Astrophysics, Flatiron Institute, 162 Fifth Avenue, New York, NY 10010
 <sup>8</sup> INAF - Astronomical Observatory of Padova, vicolo dellOsservatorio 5, IT-35122 Padova, Italy
 <sup>9</sup> Institute for Astronomy, University of Edinburgh, Royal Observatory, EH9 3HJ, UK
 <sup>10</sup> Leibniz-Institut für Astrophysik Potsdam (AIP), An der Sternwarte 16, 14482 Potsdam, Germany

#### ABSTRACT

Atomic Hydrogen (H I) is a useful tracer of gas in and around galaxies, and can be found in extended disk-like structures well beyond a system's optical extent. Here we investigate the properties of extended H I disks that emerge in six Milky Way-mass galaxies using cosmological zoom-in simulations from the Figuring Out Gas & Galaxies in Enzo (FOGGIE) suite. This paper focuses on the observability of the extended H I in these systems. We find overall agreement with observational constraints on the H I size-mass relation. To facilitate direct comparisons with observations, we present synthetic H I 21-cm emission cubes. By spatially filtering our synthetic cubes to mimic the absence of short baselines in interferometric maps, we find that such observations can miss  $\sim 10-40\%$  of diffuse emission, which preferentially removes low column density, low velocity dispersion gas outside the central disk. The amount of observable material depends strongly on its distribution and the system's observed orientation, preventing the formulation of a simple correction factor. Therefore, to fully characterize extended disks, their circumgalactic mediums, and the interfaces between them, dual convolutions including data from interferometers and large single-dish radio telescopes are required.

Keywords: Disk galaxies (391), Galaxy kinematics (602), H I line emission (690), Hydrodynamical simulations (767), Radio interferometers (1345), Circumgalactic medium (1879)

## 1. INTRODUCTION

Disks are one of the most common features of galaxies in the modern Universe. To describe a galaxy often amounts to describing its disk, and yet disks vary widely in their size, mass, thickness, kinematics, gas content, and star formation rates. Disks follow a number of well-behaved scaling relations, such as the Tully-Fisher relation between mass and rotational velocity (R. B. Tully & J. R. Fisher 1977; S. S. McGaugh et al. 2000), the Kennicutt-Schmidt relation between gas surface density and star formation rate (R. C. Kennicutt 1998), and the

Email: ctrapp2@jhu.edu

H I Size-Mass relation (J. Wang et al. 2016). Because disks are conspicuous, large, and lit up by stars, they are among the best-understood components of the cosmic baryon cycle.

Even though the bulk properties of disks are well-studied, many questions remain, and there is ample room for continued discovery. Of particular interest is the question of how galactic star formation is sustained. Gas depletion times are short ( $\sim 1~{\rm Gyr}$ ) for Milky-Way like disks (A. Saintonge et al. 2012), so in order for observed star formation rates to exist, there must be robust mechanisms that feed disks from the Circumgalactic Medium (CGM). One way to observe this material is through absorption. Astronomers seeking to explain

how extragalactic gas accretes to form disks have examined the correlations between H I disks and the CGM (S. Borthakur et al. 2015) and pursued CGM absorption observations well inside  $\sim 50$  kpc. In order to fully characterize the distribution and dynamics of this material, H I radio emission studies are necessary. The guestion of how to study this previously undetected material outside the inner disk is a difficult one. Studies utilizing large single dish radio telescopes (e.g., D. A. Thilker et al. 2004; D. J. Pisano 2014; W. J. G. de Blok et al. 2014; Q. Jiao et al. 2025) can probe low column density gas, but are lacking in spatial resolution. Interferometric emission studies (e.g., F. Fraternali et al. 2002; F. Walter et al. 2008; G. Heald et al. 2011; W. J. G. de Blok et al. 2024) provide both high spatial and spectral resolution data cubes, as well as high sensitivity, allowing for the distribution of H I to be more fully characterized. However, interferometric studies lack data from missing short baselines, meaning they are not sensitive to spatially diffuse signals greater than  $\sim 50-100$  kpc, depending on the interferometer configuration and target distance. The significance of this missing baseline effect is not well constrained in this context; however, there is little difference between the total observed fluxes between single-dish and interferometric studies. Recent studies have incorporated data from both single dish observations and interferometers, potentially alleviating this problem (e.g., C. Eibensteiner et al. 2023; J. Wang et al. 2024; E. W. Koch et al. 2025).

Cosmological, hydrodynamical simulations are another means by which we can attempt to understand the formation, evolution, and observability of gaseous disks. This paper is the second in a series of papers in which we study the extended disks, polar rings, and warps that emerge naturally for the six Milky-Way-like galaxies in the FOGGIE suite of simulations (Figuring Out Gas & Galaxies in Enzo; M. S. Peeples et al. 2019). The FOGGIE halos were selected to yield galaxies at z = 0 that resemble the Milky Way, but they were not tuned to produce extended H I disks or larger disk-like structures. Even so, all of them have extended H I at various points in their evolution. This paper focuses on the observability of these extended H I disks. To that end, we create synthetic H I 21-cm datacubes in order to draw direct comparisons with recent and upcoming observational studies. In order to investigate the effects that the missing short baselines problem has on the observability of extended H I emission, we spatially filter these datacubes to directly mimic various interferometric studies. We additionally consider the effects that viewing angle has on both the observed distribution of gas as well as observable dynamics.

The first paper in this series (C. Trapp et al. 2025) investigates the morphology and origin of the extended and misaligned H I disks in these systems, and will hereafter be referred to as FOGGIE XII.

Briefly, FOGGIE XII found that all FOGGIE H I disks have misaligned features (i.e., warps or polar rings) at some point during their evolution; however, their strengths, lifetimes, and origins vary significantly. We also found a correlation between the relative abundance of H I in the CGM and the thickness of the disk. While the six FOGGIE halos lie along a continuum of relative H I abundance, we subdivide our sample in two. The halos with relatively lower amounts of CGM H I are classified as Less Populated while the halos with higher amounts of CGM H I are classified as More Populated. The Less Populated systems form thin disks and have hot inner CGMs near their virial temperature, while the More Populated systems do not. The observational differences between these classifications will be discussed in this paper.

In Section 2 we briefly describe the FOGGIE simulations. In Section 3 we describe our disks and discuss how they broadly compare with observations. In Section 4 we detail the methodology used to create the synthetic H I datacubes. In Section 5, we discuss the effects of filtering out diffuse components on the observability of material. Finally, Section 6 discusses the effects that viewing angle has on what material is detectable in these systems and the observed dynamics.

### 2. FOGGIE SIMULATIONS

In this study, we compare six zoom-in galaxy formation simulations of Milky Way-mass halos from the Figuring Out Gas & Galaxies in Enzo (FOGGIE) suite to the latest H I 21-cm observations. The FOGGIE simulations were run using the open-source adaptive mesh refinement code Enzo (G. L. Bryan et al. 2014; C. Brummel-Smith et al. 2019). As discussed in FOGGIE XII, these simulations resolve the CGM through a novel "forced refinement" scheme, forcing high spatial resolution in diffuse gas (M. S. Peeples et al. 2019) in combination with density and cooling refinement (R. C. Simons et al. 2020). See Appendix A of FOGGIE XII for more details of the relative contributions of the refinement criteria.

These simulations have a comoving box size of  $100h^{-1}$  Mpc with a  $256^3$  root grid. The FOGGIE simulations use a forced-refinement box with a length of 288 kpc comoving on a side. Every gas cell within this box centered on and moving with the main galaxy is forced to a minimum comoving spatial resolution (1100 pc comoving). At each timestep of the simulations, cells within this box

Halo	$ m M_{200}  m M_{*,disk}$		${f M}_{ m HI,200} {f M}_{ m HI, disk}$		$\mathbf{R}_{ ext{disk}}$	$\mathbf{H}_{ ext{disk}}$	Description	
	$[10^{12}~M_{\odot}]$	$[10^{10}~M_{\odot}]$	$[10^{10}~M_{\odot}]$	$[10^{10}~M_{\odot}]$	$[\mathrm{kpc}]$	$[\mathrm{kpc}]$		
Less Populated								
Tempest	0.50	4.02	1.28	1.27	21.8	1.25	$Strong\ warp$	
Maelstrom	1.01	7.24	2.72	2.36	24.2	0.69	$Thin\ disk$	
Blizzard	1.14	9.02	2.79	2.33	22.0	0.69	$Strong\ warp$	
More Populated								
Cyclone	1.69	17.41	3.88	3.17	38.2	2.36	$Polar\ ring$	
Hurricane	1.71	17.20	3.73	2.94	33.3	0.69	$Two\ polar\ rings$	
Squall	0.80	10.48	0.73	0.50	16.8	1.81	Misaligned inner disk	

**Table 1.** Key properties and brief description of the FOGGIE halos at z=0

Note—The masses shown are either the mass within  $R_{200}$  (e.g.  $M_{\rm HI,200}$ ), or the mass within our disk definition (e.g.  $M_{\rm HI,disk}$ ). The difference between these two corresponds to the H I mass in the CGM.  $R_{200}$  is the radius enclosing an average density of  $200\times$  the critical density of the universe at z=0.  $R_{disk}$  is the radius at which the mean H I column density falls below  $1.25\times10^{20}~{\rm cm}^{-2}$ , a commonly used observational contour (e.g., J. Wang et al. 2016; J. Blue Bird et al. 2020).  $H_{disk}$  is the H I scale height. We divide our sample into two based on the relative abundance of H I in their CGMs. Less Populated systems have little H I in their CGMs relative to the central disk and, therefore, a lower amount of diffuse signal compared to the More Populated systems. Less Populated systems form thin disks and have an inner CGM near their virial temperature; More Populated systems do not.

are allowed to further refine based on density. This generation of FOGGIE simulations implemented a "cooling refinement" criterion to better resolve thermally unstable gas. This criterion refines cells such that their size is smaller than the cooling length (sound speed  $\times$  cooling time). The density and cooling refinement criteria are allowed to resolve up to 274 pc comoving.

This forced refinement scheme is of particular importance in the context of extended H I emission, as the spatial scales of low column density gas outside the main disk are only now starting to be constrained. Many of these observational studies are conducted with interferometers, which are only sensitive to spatial scales up to a maximum angular size limit, determined by their shortest baseline. Importantly for this study, the largest permitted cell size in the forced refinement region  $(1.1 \, \text{kpc comoving})$  is much smaller than the largest relevant angular scale for these interferometers, for typical distances (e.g.,  $\sim 60 \, \text{kpc}$  for the 21-cm line at 10 Mpc).

The FOGGIE simulations have predicted direct observables for a range of CGM and galaxy topics. These include: absorption (M. S. Peeples et al. 2019) and emission lines (L. Corlies et al. 2020, C. Lochhaas et al. 2025, V. Saeedzadeh et al., in prep), absorption-line observations of the CGM of the Milky Way (Y. Zheng et al. 2020), and the interface between galaxies and the intergalactic medium (N. Lehner et al. 2022).

In this study, we analyze all six halos in the second generation of FOGGIE simulations near redshift z=0. All halos were selected to be Milky Way-like at z=0 in terms of their mass and merger history (see A. C. Wright et al. 2024). After z=2, there are no major mergers with the exception of Squall, which experiences a 2:1 merger at z=0.7. For a more detailed analysis of the evolution of these halos' H I profiles over time, see FOGGIE XII.

### 3. DISK PROPERTIES

Table 1 presents basic properties of the sizes and masses of these systems. In order to calculate disk masses, we use our disk defintion introduced in FOG-GIE XII. In brief, we define the disk as a contiguous region with H I number density above  $\sim 6 \times 10^{-3} \ {\rm cm}^{-3}$  at z=0. To avoid missing low-density regions in the disk associated with stellar feedback or dynamical effects, we fill both fully enclosed holes and "donut" holes that completely pierce the disk.

As previously mentioned, we divide the halos into broad categories based on the amount of H I in their CGM relative to the central disk. The Less Populated systems (Tempest, Maelstrom, and Blizzard) have a relatively small amount of H I in their CGMs, form thin disks, and have hot inner CGMs near their virial temperature at z=0. Tempest is the smallest system by mass, and shows little H I outside its central disk ( $\sim 10^8$ 

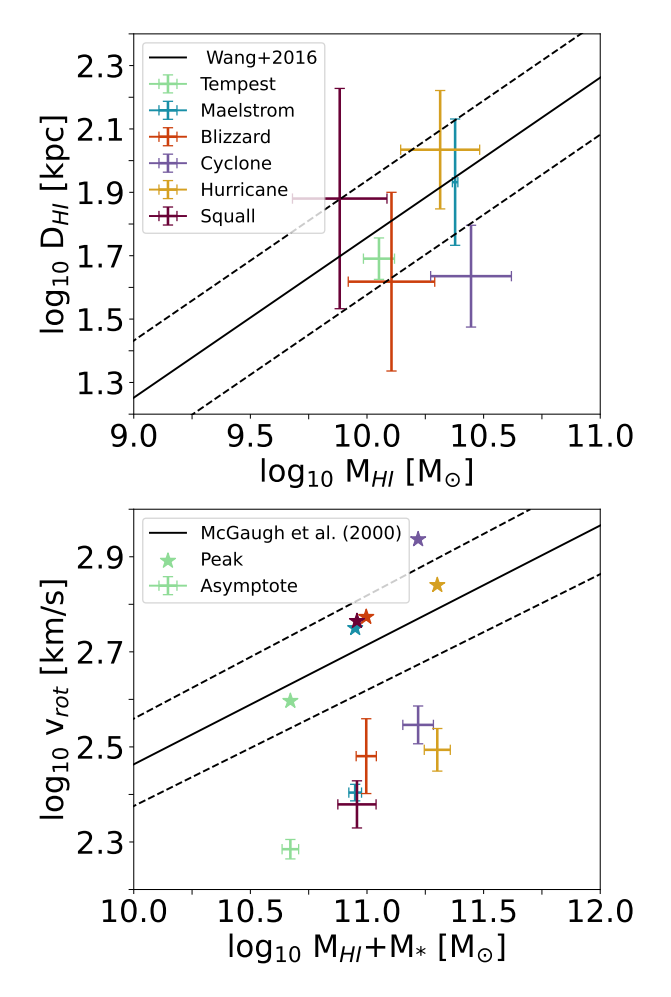


Figure 1. Scaling relations for the six H I disks presented in this study. The points correspond to the mean values for a given system between z = 0 and z = 0.5, with bars showing the standard deviation. Top: The H I Size-Mass relation (A. H. Broeils & M. H. Rhee 1997a) for these systems.  $M_{HI}$  is calculated as the total disk H I mass.  $D_{HI}$ is twice the radius at which the mean column density drops below  $1.25 \times 10^{20}$  cm<sup>-2</sup>. The solid (dashed) line corresponds to the observational correlation (and  $3\sigma$  scatter) found in J. Wang et al. (2016). Bottom: The Baryonic Tully-Fisher relation.  $M_*$  is calculated as the stellar mass within the disk. We plot the median values of the density-weighted rotational velocity curve, as it best approximates an asymptotic value. All six systems fall below the observed relation (S. S. Mc-Gaugh et al. 2000), although they show similar trends with increasing mass. The additional points (stars) denote the time-averaged peak of the rotational velocity curves, which align more closely.

 ${\rm M}_{\odot}$ ). It shows a strong warp (inclination of  $\sim 20^{\circ}$ ) at redshift z=0. Maelstrom has more H I mass in its CGM ( $\sim 3.6 \times 10^9 {\rm M}_{\odot}$ ), but is less populated in comparison to other systems. It does not have a significant warp at z=0. Blizzard has a more significant amount

of H I in its CGM ( $\sim 4.6 \times 10^9 \text{ M}_{\odot}$ ) as well as a strong warp at redshift z = 0 (inclination of  $\sim 20^{\circ}$ ).

The More Populated systems (Cyclone, Hurricane, and Squall) have relatively more H I in their CGMs, do not form thin disks, and have cooler inner CGMs at z=0. Despite having a large stellar mass, Squall has relatively little H I in its disk, although there is a relatively large amount in its CGM ( $\sim 2.3 \times 10^9 \text{ M}_{\odot}$ ). At z = 0 it has a small ( $\sim 2$  kpc), misaligned inner disk. Hurricane is the most active system and has a relatively large amount of H I outside its central disk ( $\sim 7.9 \times 10^9$  $M_{\odot}$ ). Additionally, it has two distinct polar rings at z=0. Cyclone has a nearly perfectly orthogonal polar ring, as well as a large amount of CGM material. For a more detailed analysis of the properties, origins, and evolution of these misaligned features, as well as how this categorization relates to disk morphology and thin disk formation, see FOGGIE XII.

Observations of H I disks find a tight correlation between the observed H I mass and the spatial size of the H I disk (e.g., A. H. Broeils & M. H. Rhee 1997b; J. Wang et al. 2016; J. Blue Bird et al. 2020). A commonly used metric is the correlation between the H I mass of the galaxy and the diameter of the  $N_{HI}=1.25\times 10^{20}~{\rm cm^{-2}}$  contour. The top panel of Fig. 1 shows this relation for the six halos considered in this study from redshift z = 0 - 0.5. This redshift range was chosen to match the redshift range of the CHILES survey (J. Blue Bird et al. 2020), which has galaxies that closely follow this relation with  $D_{HI}$  ranging from a few kpc to  $\sim 60$  kpc. The points represent the mean values between these redshifts, with the bars showing the standard deviation. The H I mass,  $M_{HI}$  is the total within the defined disk region. The disk diameter,  $D_{HI}$ , is calculated as two times the radius at which the mean face-on column density drops below  $1.25 \times 10^{20} \ \mathrm{cm^{-2}}$ . All the Less Populated systems (Tempest, Maelstrom, and Hurricane) fall within the observed scatter from J. Wang et al. (2016). Squall and Blizzard are on the upper and lower edges, respectively. Cyclone is overmassive for its size. This is likely due to its recent interaction history with satellite galaxies, leading to a relatively large amount of material in the CGM and a relatively compact disk.

The bottom panel of Fig. 1 shows the Baryonic Tully-Fisher Relation, which relates the total mass of baryons in a system to the asymptotic rotational velocity (S. S. McGaugh et al. 2000). Star formation in this generation of the FOGGIE galaxies is overly concentrated in the centralmost regions (A. C. Wright et al. 2024), leading to sharply peaked rotation curves. When comparing the median rotational velocities, none of the galaxies in

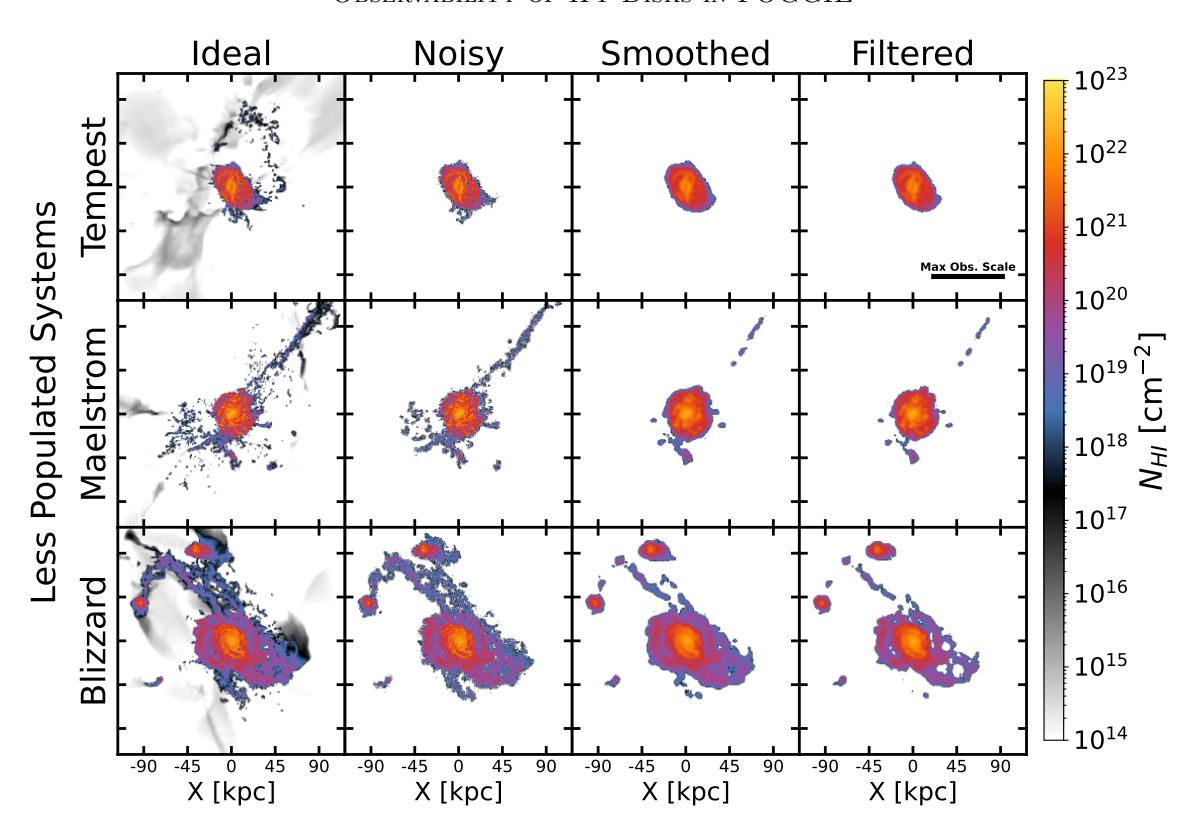


Figure 2. Effects of various steps of the synthetic H I imaging pipeline for the three Less Populated galaxies at 10 Mpc at an inclination of 40°. Imaging parameters are selected to be analogous to lower resolution, high sensitivity MeerKAT observations (i.e., sensitivity = 10<sup>18</sup> cm<sup>-2</sup>, beam size = 65", minimum baseline length = 35 m). The scale bar on the top right shows the maximum observable angle at this minimum baseline. The first column (Ideal) shows the ideal column density projections. The second column (Noisy) adds Gaussian noise with a standard deviation equal to 0.2 times the sensitivity limit. For this column and the final two, only sources identified as significant are plotted. The third column (Smoothed) shows the effects of a Gaussian smoothing kernel being applied to the data, which removes signals with small spatial scales. The final column (Filtered) shows the effect of spatially filtering the data. The three galaxies presented respond to this step in distinct ways, related to how much diffuse gas is present around the disk. This has little effect on Tempest and Maelstrom, but has a larger effect on Blizzard due to the presence of more diffuse signal.

our sample fall within the observed scatter. When comparing the peak rotational velocities (near the galactic center), all systems except for Cyclone follow the relation.

### 4. SYNTHETIC H I 21-cm OBSERVATIONS

In this section, we investigate the observability of the H I distributions presented in this study via the creation of synthetic H I 21-cm emission cubes. Importantly, when the effects of missing short baselines are considered, the observed distribution of H I changes significantly based on the survey parameters and galaxy.

In order to draw comparisons with multiple H I 21-cm surveys, we created synthetic datacubes for all six of our halos with a variety of instrumental parameters. The parameters that varied between the synthetic surveys were: spatial resolution, spectral resolution, primary beam full-width half-max (FWHM), minimum baseline length, and sensitivity. For our fiducial suite of synthetic

images, we considered all systems at an observed inclination of 40° and a distance of 10 Mpc. Both distance and inclination can have effects on the observability of specific H I components, however, we chose these values to best match surveys such as THINGS (F. Walter et al. 2008) and MHONGOOSE (W. J. G. de Blok et al. 2024).

The dimensions of the final image were selected such that the point spread function of the synthetic survey is oversampled by a factor of four and the field-of-view (FOV) is comparable to the large FOV of the MHON-GOOSE survey (350 kpc). In order to capture the high rotational velocities in the central regions of the FOG-GIE disks, we increased the bandwidth beyond survey parameters as needed for each system.

To create our synthetic datacubes, we considered all grid cells containing non-zero H I gas mass within the forced refinement region (288 kpc comoving on a side) of the simulation. Gas outside this region was not con-

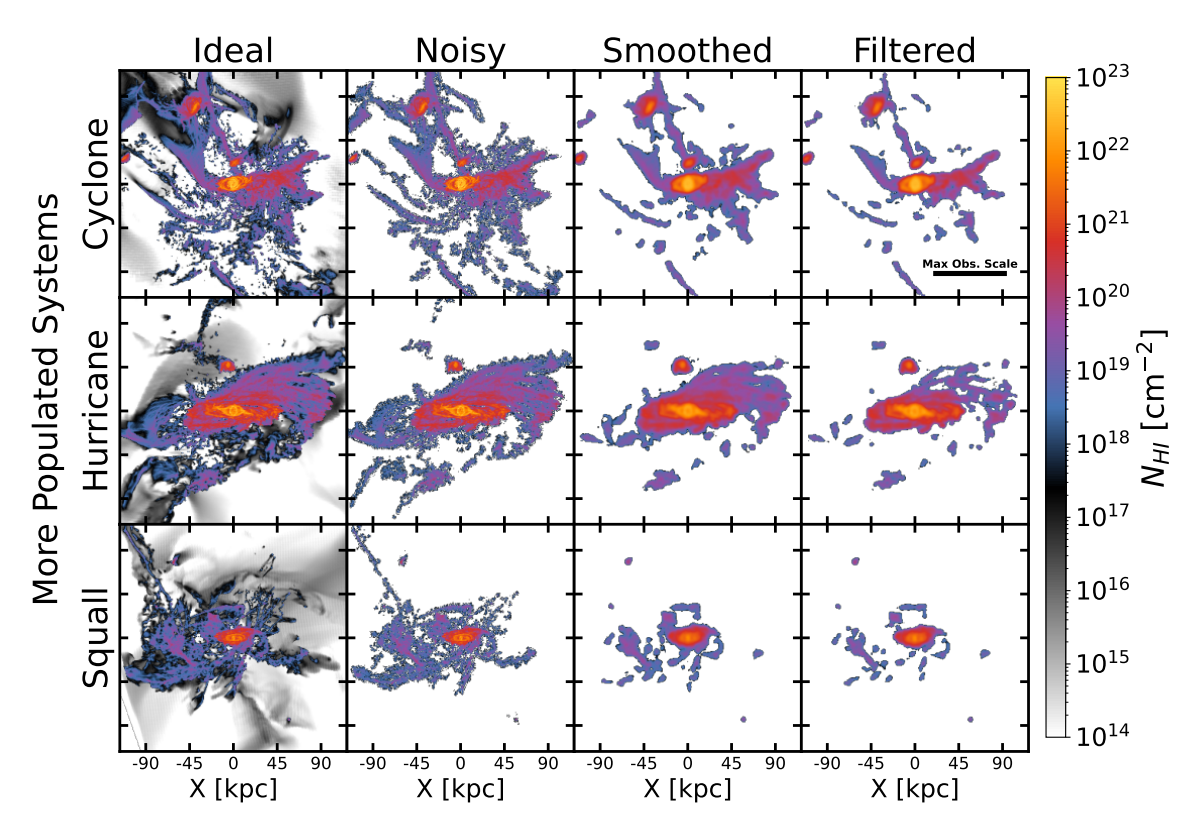


**Figure 3.** Same as Fig. 2, but for the three *More Populated* systems. These systems have a much larger amount of both small-scale and diffuse material in the CGM that is lost in the smoothing and filtering steps, respectively.

sidered, due to its poorer spatial and mass resolution. The Voigt profiles, including Gaussian core and damping wings, were then calculated for each cell. The flux densities were normalized by the cells' column density and projected onto the final image as follows:

$$\frac{F_{\nu,cell}}{\text{cm}^{-2} \text{ s}} = \left(\frac{M_{\text{HI},cell}}{m_{\text{HI}}}\right) \left(\frac{l_{cell}^{-2}}{\text{cm}^{-2}}\right) \left(\frac{\phi_{\nu,cell}^{Voigt}}{\text{s}}\right) \tag{1}$$

where  $M_{\mathrm{HI},cell}/m_{\mathrm{HI}}$  is the number of H I atoms,  $l_{cell}$  is the cell size, and  $\phi_{\nu,cell}^{Voigt}$  is the normalized Voigt profile for the cell at its Doppler velocity. We assume the gas is optically thin (M. A. Zwaan et al. 1997; F. Walter et al. 2008), so the H I flux and mass differ only by a constant factor. While this assumption may break down in the interstellar medium, it holds in the CGM. We therefore left our datacubes in units of cm<sup>-2</sup> s for simplicity, such that the integration over all channels gives the H I column density.

This gives us the "ideal" datacube. In order to make full mock spectra, we further degrade the images in a few steps: adding the effect of the primary beam, smoothing spatially, adding noise, and filtering out low spatial frequencies. The effects of each step are visualized in Fig. 2 and Fig. 3.

We model the primary beam (which effectively sets the field of view) as a Gaussian with a FWHM equal to  $0.5^{\circ}$  (VLA) or  $1^{\circ}$  (MeerKAT), depending on the specific survey being targeted. This lowers the signal at the edge of the field of view.

The effective column density sensitivity of the study is determined by the strength of the noise we add. To create our "noisy" datacube, we model the noise as a Gaussian noise distribution with a standard deviation equal to 0.2 times the synthetic survey column density limit, such that  $5\sigma$  detections correspond to the sensitivity limit. Under the assumption that the noise is largely uncorrelated with the signal (S. Veronese et al. 2025), we create this noise cube separately and added it to the ideal datacube.

In order to smooth the data, we convolve the ideal data cube and noise cube with a Gaussian beam. The FWHM was set to the effective spatial resolution of the synthetic survey, and the noise cube was rescaled as necessary to match the target sensitivity. This gave us our "smoothed" datacube.

Finally, we consider the effect that missing short baselines has on filtering out diffuse signals. Each baseline in an interferometric survey samples a specific location in spatial frequency space (the UV plane). Longer baselines sample high spatial frequencies, while shorter baselines sample lower spatial frequencies. Interferometers are limited by their lack of zero distance baselines, mean-

	$MHONGOOSE-LR$ $\sigma = 65''$ $b_{\min} = 29 \text{ m}$ $N_{\text{HI}} = 1 \times 10^{18} \text{ cm}^{-2}$		MHONGOOSE-HR		THINGS		SKA	
			$\sigma = 22''$		$\sigma = 6''$		$\sigma = 22''$	
			$b_{\min} = 29 \mathrm{m}$		$b_{\min} = 35 \mathrm{m}$		$b_{\min} = 29 \mathrm{m}$	
Halo			$N_{\rm HI} = 5 \times 10^{18}  \rm cm^{-2}$		$N_{\rm HI} = 1 \times 10^{19}  \rm cm^{-2}$		$N_{\rm HI} = 2.5 \times 10^{17}  \rm cm^{-2}$	
	Smoothed	Filtered	Smoothed	Filtered	Smoothed	Filtered	Smoothed	Filtered
Less Populated								
Tempest	0.000	0.000	0.000	0.000	0.000	0.000	0.722	0.0759
Maelstrom	0.545	0.352	0.399	0.190	0.362	0.312	0.908	0.808
Blizzard	0.887	0.516	0.724	0.431	0.669	0.429	0.986	0.792
$More\ Populated$								
Cyclone	0.845	0.587	0.698	0.519	0.592	0.411	0.969	0.826
Hurricane	0.896	0.500	0.849	0.548	0.663	0.501	0.981	0.802
Squall	0.530	0.305	0.239	0.158	0.208	0.132	0.922	0.681

Table 2. Ratio of observable H I mass in the CGM to actual H I mass for different survey parameters

NOTE—The three survey parameters varied are: the effective angular resolution ( $\sigma$ ), the minimum baseline length simulated ( $b_{\min}$ ), and the H I column density sensitivity ( $N_{\rm HI}$ ). The first two columns are analogous to two of the resolutions available in the MHONGOOSE survey (W. J. G. de Blok et al. 2024): Low-Resolution (LR) and High-Resolution (HR). The third column is analogous to the THINGS survey (F. Walter et al. 2008). The final column is analogous to what may be seen with the fully realized Square Kilometer Array (SKA). All surveys are able to observe almost all H I gas inside the disk (within 1–2%). Depending on the specific system, however, survey parameters perform drastically differently in recovering the CGM gas mass, with the spatial filtering step reducing recoverable CGM emission by  $\sim 10\%$ –40%. The final column, analogous to what may be visible with the SKA, performs the best for each system. Of the other surveys, performance depends on the relative abundance of diffuse and compact components in the CGM. Values are calculated without satellite contribution.

ing they are missing out on the most diffuse signals. In order to fully investigate the theoretical observability of the gas in our halos, we simulate this effect in a conservative way.

To start, we apply a Fast-Fourier Transform (FFT) to each spectral slice and then apply a Gaussian high-pass filter to remove the low spatial frequency components. The FWHM of the high-pass filter is set equal to the minimum observable spatial frequency for a given minimum baseline. The selection of the Gaussian high-pass filter as opposed to a sharper filter was made to minimize any ringing artifacts in the resulting image. We also did not consider any sparse sampling of the rest of the UV plane, meaning we are retaining more UV points than an actual interferometer would.

Despite using a Gaussian high-pass filter, significant filtering artifacts were still introduced due to the tight cutoff imposed by the short baselines sampled by instruments such as MeerKAT or the Very Large Array (VLA) in C/D configuration. To extract all significant signal, we transformed the filtered images back into image space and deconvolved the resulting dirty images with the Högbom CLEAN algorithm (J. A. Högbom 1974). The beam was modeled on an ideal calibrator (a single pixel of value unity at the center of the FOV).

Each slice was cleaned individually down to  $3\sigma$ , where  $\sigma$  is the noise level in the dirty image. This cutoff was chosen empirically, as it retrieves the most signal without creating erroneous noise sources. It is also a typical cleaning depth used in observational surveys (F. Walter et al. 2008; W. J. G. de Blok et al. 2014). The sum of the CLEAN components and the residuals was used to create our "filtered" datacubes.

The final step in our synthetic datacube pipeline is the creation of source masks to identify spaxels with statistically significant signal. This was done using the SoFIA-2 software package (T. Westmeier et al. 2021). Parameters were chosen to mimic the corresponding observational surveys (W. J. G. de Blok et al. 2024). In brief, we use the SoFiA-2 "smooth and clip (S+C)" method using spatial kernels of 0 and 4 pixels, velocity kernels of 0, 9, and 25 channels, and a threshold of  $5\sigma$ . Kernel sizes were adjusted for other surveys as necessary.

We chose four different combinations of parameters to target four different synthetic surveys. These parameters are summarized in Table 2. The first two are analogous to the MHONGOOSE survey at two different resolution targets: low-resolution (MHONGOOSE-LR) and high-resolution (MHONGOOSE-HR) (W. J. G. de Blok et al. 2024). The third survey is analogous to

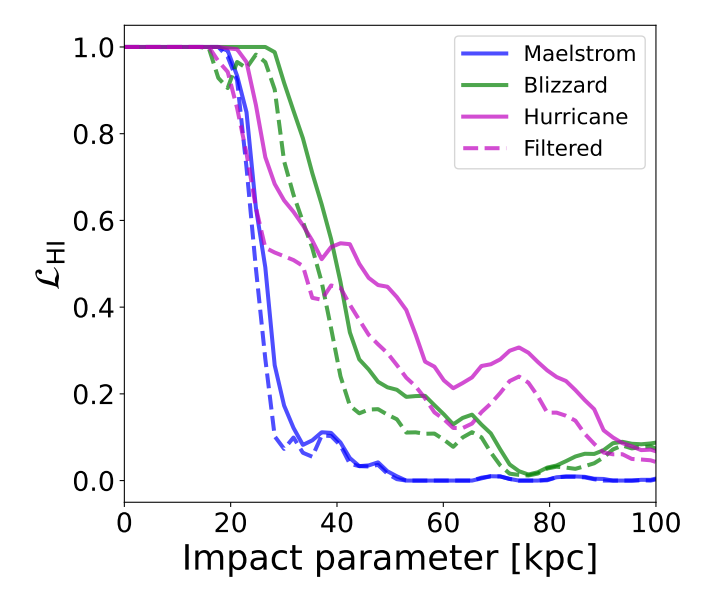


Figure 4. H I covering fraction  $(\mathcal{L}_{HI})$  as a function of impact parameter for the "smoothed" (solid) and "filtered" (dashed) moment-0 maps shown in Fig. 2 and Fig. 3. As expected, the curve for Maelstrom does not change significantly, as there is little diffuse material that is filtered out. For both Blizzard and Hurricane, the filtered curve is shifted to the left by a few kpc due to diffuse material being filtered out. Covering fractions are calculated in a 2 kpc thick annuli centered on the given impact parameter.

the THINGS survey (F. Walter et al. 2008). The final survey is analogous to the future Square Kilometer Array (SKA).

# 5. THE EFFECTS OF FILTERING OUT DIFFUSE COMPONENTS

Fig. 2 and Fig. 3 show the effects that each step of our synthetic imaging pipeline has on the column density projections (moment 0 map). These figures mimic the MHONGOOSE survey's low-resolution case (beam FWHM = 65", sensitivity  $\sim 10^{18}~\rm cm^{-2}$ , primary beam FWHM = 1°, W. J. G. de Blok et al. 2024). Of particular interest is the difference between how diffuse and compact components respond to various steps.

The first column ("ideal") shows the ideal datacube at the target pixel resolution. The second column ("noisy") shows the effect of the column density cutoff imposed by the noise parameter. This step cuts out most of the diffuse gas. The third column ("smoothed") shows the effect of the Gaussian smoothing. Aside from the obvious degradation of the spatial resolution, this also has the effect of reducing some small spatial scale signals below the column density sensitivity. The fourth column ("filtered") shows the effects of the spatial filtering and cleaning. Diffuse components on the scale of the maximum observable size are filtered out. The disk itself

is largely unaffected, however, the emission at the disk edge and in the CGM is reduced. For Maelstrom and Tempest, which do not have much detectable diffuse gas at this sensitivity, there is little effect. For the other halos, there are more significant effects due to the presence of more diffuse, high column density gas in these systems.

Fig. 4 shows the covering fraction of the smoothed and filtered images as a function of impact parameter for three representative halos with the MHONGOOSE-LR survey parameters. For Maelstrom, there is little difference between the two curves. For Blizzard and Hurricane, however, the filtered curve is shifted inwards by a few kpc. This implies that for systems with more diffuse extended emission, such as is seen in the *More Populated* systems and Blizzard due to its more recent interactions, interferometric studies may be underestimating disk sizes by up to  $\sim 5$  kpc. This reduction in observed size will only occur when there is a significant amount of spatially diffuse signal at the disk edge above the column density limit, and is therefore highly galaxy-dependent.

The quantitative effects of the smoothing and filtering steps are shown in Table 2. This table shows the observable mass fractions (ratio of the mass in the smoothed/filtered images versus the ideal images). Each row shows only the mass ratio for the CGM, with the contributions from the disk and satellites filtered out. The detectable H I emission from the disk (and therefore the system as a whole) is largely unaffected by both the smoothing and spatial filtering steps, with each survev able to detect at least  $\sim 98\%$  of the HI. The disk is masked out using our disk definition (see FOGGIE XII) projected onto the image and smoothed at the target survey resolution. The disk removal is based on the full 3D gas distribution in the simulation and does not depend on the chosen line of sight. To mask out the satellites, we initially identify subhalos via ROCKSTAR, and then mask them out using the same method as was used for the central disk.

For most systems, the filtering step reduces the observable CGM H I mass by  $\sim 10$ –40%. Tempest is a unique case, as most of its CGM H I is in small-scale clumps that are not detected by most survey parameters. The first two columns are analogous to the MHONGOOSE survey at two different resolution targets (W. J. G. de Blok et al. 2024). The third column is analogous to the THINGS survey (F. Walter et al. 2008). The survey on the far right is an analogue to the Square Kilometer Array, and performs the best in all cases. The relative performance of other surveys varies

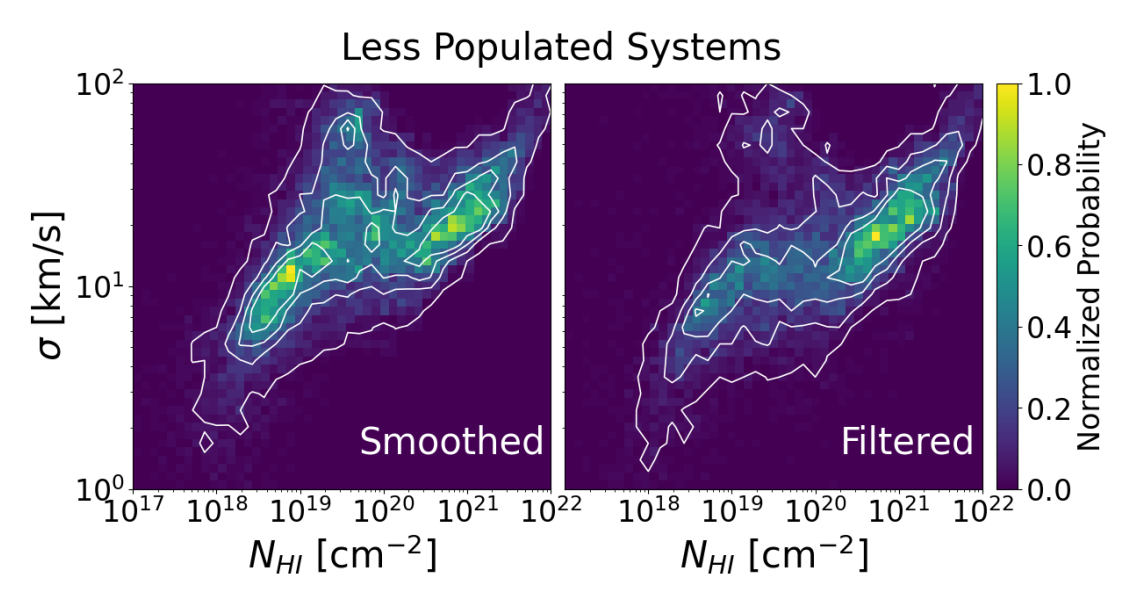
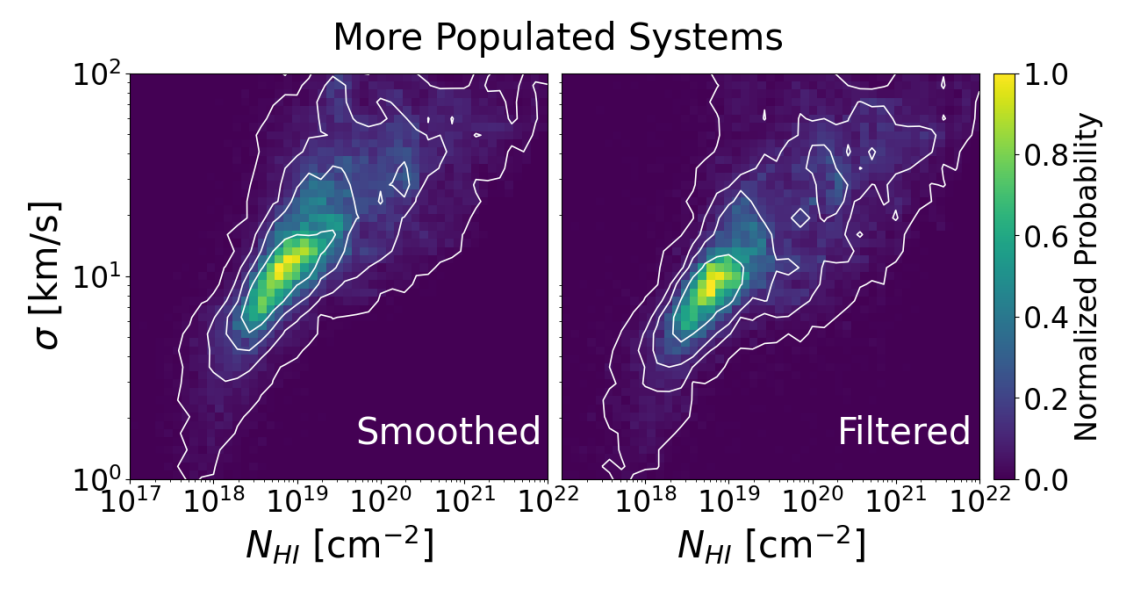


Figure 5. Log histogram of H I column density  $(N_{HI})$  versus velocity dispersion  $(\sigma)$  summed for the three Less Populated systems (Tempest, Maelstrom, and Blizzard).  $N_{HI}$  was corrected for inclination (i) by a factor of  $\cos i$ . The color scale shows the normalized probability distribution of pixels. The contours show the 25th, 50th, 75th, and 95th percentile curves. The synthetic survey parameters are analogous to the MHONGOOSE survey's low-resolution case (beam FWHM  $\sim 65$ ", sensitivity  $\sim 10^{18}$  cm<sup>-2</sup>, minimum baseline = 29 m). The plot on the left shows the distribution for the smoothed datacube (without filtering). There are two peaks in the distribution: high column density and high velocity dispersion gas in the top right, and low column density and lower velocity dispersion gas in the bottom left. The plot on the right shows the same distribution for the filtered datacubes. The high column density peak is largely unaffected; however, the low column density peak is greatly reduced by the filtering step. This implies that this gas is primarily diffuse and may not be visible to interferometric observations.



**Figure 6.** Same as Fig. 5, but for the *More Populated* systems (Cyclone, Hurricane, and Squall). The low column density peak in these systems is much more dominant. While this peak is reduced during the filtering steps, the effect is less dramatic than in the *Less Populated* systems.

system by system and depends on the spatial scales of the CGM gas.

Fig. 5 shows 2-D histograms of the column density versus velocity dispersion of each pixel in the smoothed and filtered images for the three *Less Populated* halos in our sample (Tempest, Maelstrom, and Blizzard) for the MHONGOOSE-LR survey parameters. The histograms for the smoothed datacubes show two peaks at high and low column densities. The low-column-density peak is not seen in observations, despite being present in other

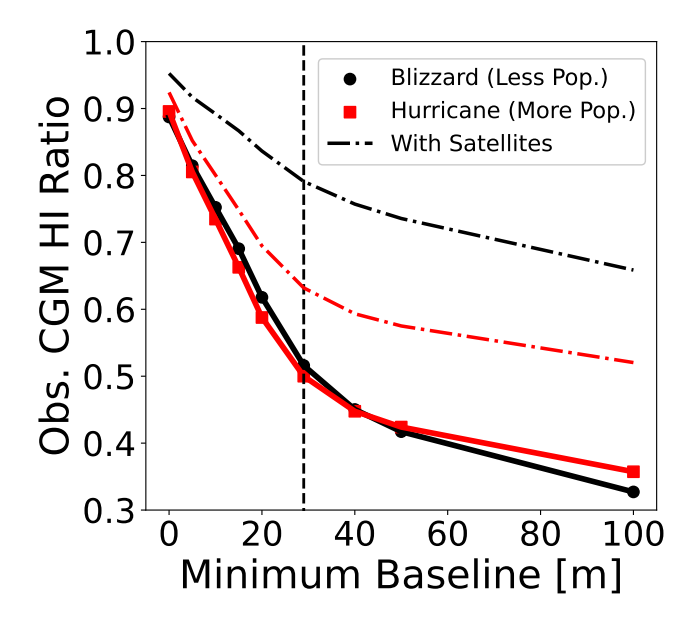


Figure 7. Evolution of how much H I emission in the CGM is observable as a function of minimum baseline. The rest of the survey parameters are analogous to the MHON-GOOSE survey's low-resolution case (beam FWHM  $\sim 65^{\circ}$ , sensitivity  $\sim 10^{18}$  cm<sup>-2</sup>). Solid lines show the CGM ratio with satellites removed, while the dash-dotted lines show the ratio with satellites present. The vertical dashed line shows the MeerKAT minimum baseline ( $b_{min} = 29$  m). An observation with this minimum baseline potentially misses 50% of the CGM H I that is present. With satellites removed, observing  $\sim 90\%$  of the CGM signal would require minimum baselines of a few meters, likely requiring dual convolution with single dish observations.

simulations (A. Marasco et al. 2025). The histograms for the filtered data cubes show a much-reduced peak, implying that this gas may not be detected in interferometric studies. Fig. 6 shows the same 2-D histograms for the More Populated systems, which show relatively lower column density, low velocity dispersion gas in both cases. The overall filtering effect of reducing this peak is the same, although the low column density peak is still dominant. The diffuse gas in these systems, despite having relatively little mass compared to the central disks, occupies large volumes and is, therefore, represented by a large number of cells in the simulation and spaxels in the resulting H I datacubes. This causes the low column density peak to remain dominant over the higher column density peak. The removal of satellites has little to no effect on these plots.

Finally, Fig. 7 shows how the observable CGM H I ratio depends on the minimum baseline length for Blizzard and Hurricane. All other survey parameters match the MHONGOOSE-LR survey. In order to recover at least 90% of the signal a minimum baseline of less than 5 m

would be required. The points at 0 m represent what can be observed at the given sensitivity limit for the given smoothing. Given that dish sizes for the VLA and Meerkat are 25 m and 13.5 m, respectively, such small baselines are unrealistic. Dual convolutions with single dish data are therefore needed to recover this signal.

### 6. EFFECTS OF VIEWING ANGLE

The observed viewing angle can have significant effects on what information can be reliably inferred from observation. The most salient effect is the inclination of the system towards or away from the observer. This readily affects the observable structure of the galaxy (i.e., edge-on versus face-on) as well as the relative strengths of various velocity components (e.g., rotational velocity is easier to measure in highly inclined disks, while vertical velocities are easier to measure in less inclined disks). The observed position angle versus the direction of the misalignment is of particular importance when considering misaligned gas, as is seen in the outer disks of many of our systems, as well as their CGMs. In this section, we discuss specifically how these effects relate to the observed spatial scales on the sky and their consequences for observability in interferometric studies, as well as how these misaligned features may manifest dynamically at a variety of viewing angles with Blizzard and Tempest as case studies.

For this section, we discuss two viewing angles: inclination (i) and position angle (PA). The inclination angle describes the tilt of the disk towards or away from the observer, with a value of  $i = 90^{\circ}$  corresponding to an edge-on view, and a value of  $i = 0^{\circ}$  corresponding to a face-on view. In a coordinate system with the z-axis defined by the rotational axis of the disk, this inclination angle is equivalent to the pitch of the system. The position angle describes the rotation around the the z-axis, equivalent to the yaw of the system. In a cylindrically symmetric system, this position angle would have little to no effect. In systems with misaligned extended disks and CGMs, the position angle can affect the projected spatial scale and observed dynamics, as discussed below. These angles can be visualized in the projections on the top and right of Fig. 8.

The projected spatial scale of the H I on the sky is highly relevant to the study of extended H I distribution with radio interferometers. For a well-defined, disky system, an edge-on (high inclination) view will have relatively small spatial scales. A face-on view (low inclination), on the other hand, will take up a larger portion of the sky. Fig. 8 shows how the observable H I ratio in the CGM varies with both inclination and position angle for Blizzard. As expected, the observable ratio generally

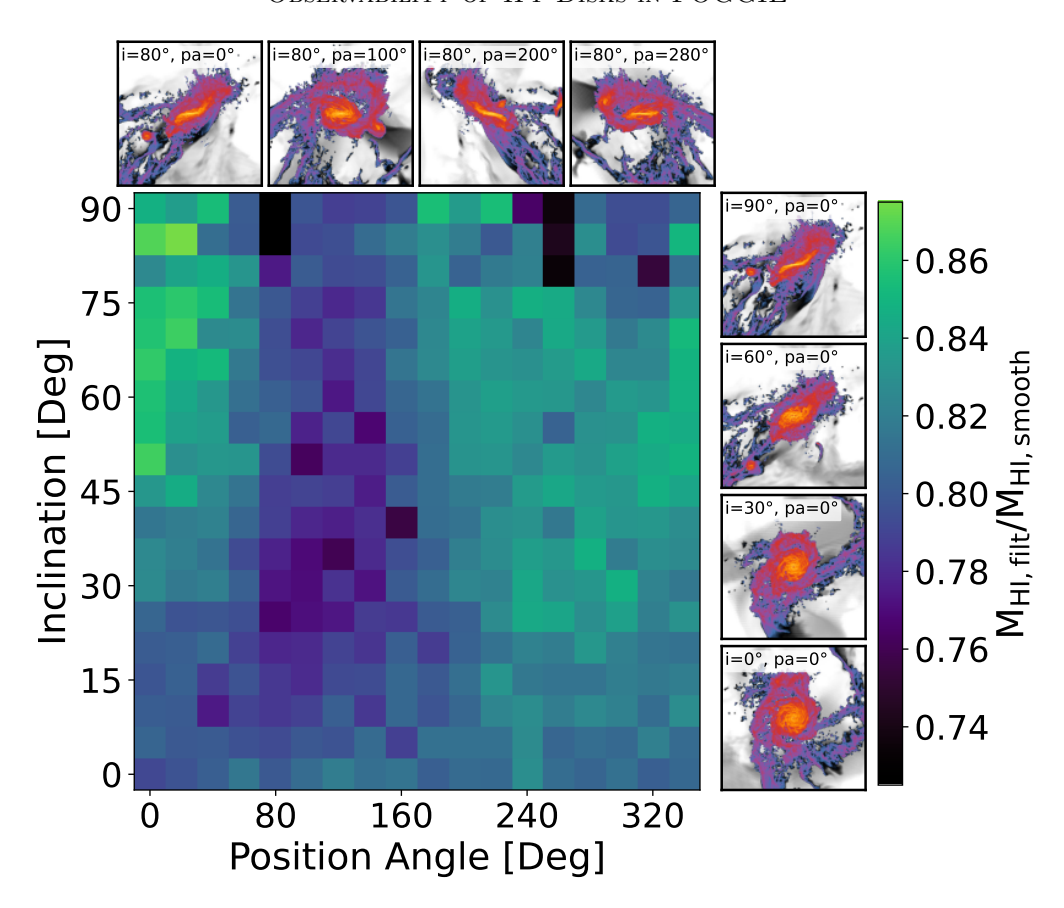


Figure 8. Ratio of observable H I in the filtered image to observable H I in the smoothed image for Blizzard at various observed inclinations and position angles (at z=0). This isolates the effect of missing short baselines. Imaging parameters correspond to MHONGOOSE-LR. Projections on the top and right show the ideal H I column density maps at various orientations. There is a general increase in this ratio at higher inclination, as edge-on galaxies appear more compact on the sky. At lower inclinations, there is little dependence on position angle; however, there is a clear pattern at higher inclinations. When the galaxy is more edge-on, there are two regions of lower observability at position angles of  $\sim 100^{\circ}$  and  $\sim 280^{\circ}$  corresponding to when the warped component of the disk is face-on with the observer, causing dips in the observable CGM ratio.

increases with increasing inclination, as the edge-on projection is more compact and therefore there is less spatially diffuse signal that is lost to the missing short baseline problem. This is complicated by the significant warp in the outer disk of Blizzard. This results in a significant evolution with position angle at intermediate and high inclinations. At low inclinations ( $\sim 0^{\circ}-15^{\circ}$ ), there is little evolution with position angle. What evolution there is is likely caused primarily by field of view effects. At intermediate inclinations ( $\sim 15^{\circ}-75^{\circ}$ ), there is a region of lower observability around PA=100°. At high inclinations (~75°-90°), a second region of lower observability appears around PA=280°. These position angles correspond to where the warp of Blizzard is more face-on, causing it and kinematically aligned CGM gas to take up larger spatial scales in the sky. Further misalignment of the CGM gas exaggerates this effect at PA=100°, while limiting it at PA=280° in this case. This trend with inclination is present in the rest of the systems, and

the trend with position angle is similar in other systems with misaligned features. We specifically do not remove satellites from this plot, to avoid confusion masking out different physical regions in different projections. Overall trends remain the same.

Fig. 9 shows how the ideal first moment maps for Tempest vary as a function of observed position angle at a fixed inclination (20°). The choice of position angle=0° is arbitrary and was chosen such that the warp orientation (dashed line) was left to right at PA=0°. The large vertical velocities associated with the orbits of gas in the warp appear as a deviation from the dipole signature associated with disk rotation. The strength and sign of this deviation depend primarily on the angle between the warp axis and the observed kinematic axes of the galaxy. When the warp is aligned with the disk major axis (PA=270°), there is no qualitatively noticeable effect, although the projected velocities increase at the warp. When the warp is more aligned with the disk mi-

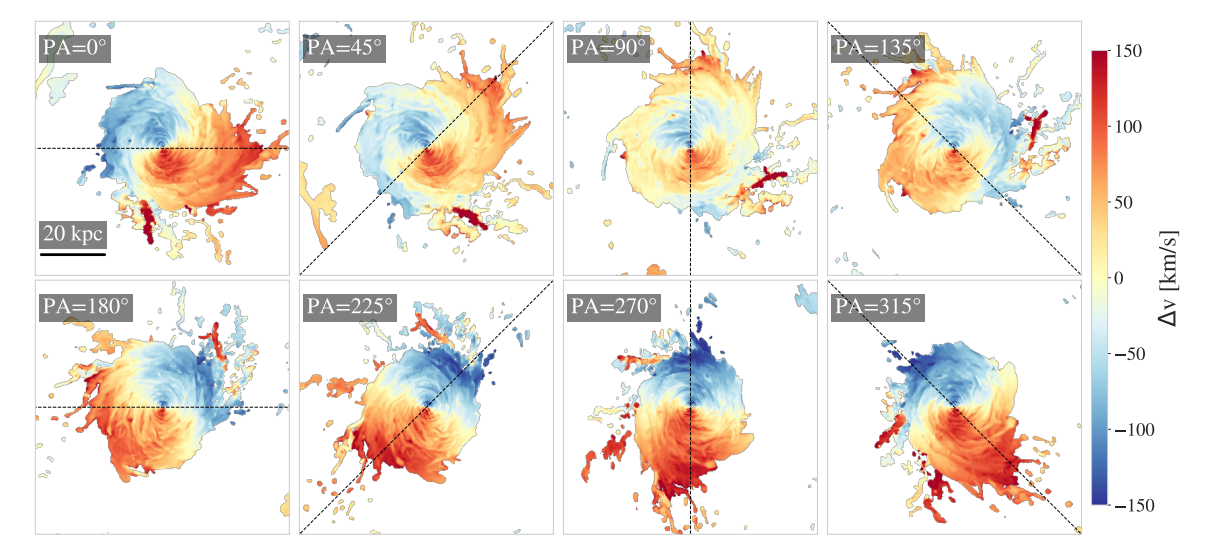


Figure 9. Ideal first moment maps (projected velocity component) for Tempest at various position angles. Only pixels above  $N_{HI} > 10^{16}$  cm<sup>-2</sup> are shown for visual clarity. All images are projected at an inclination of 20° at redshift z = 0. The black dashed line shows the direction of the warp, fit by eye. The warp causes what appear to be velocity inversions when it is anti-aligned with the observed disk major axis (PA=90°).

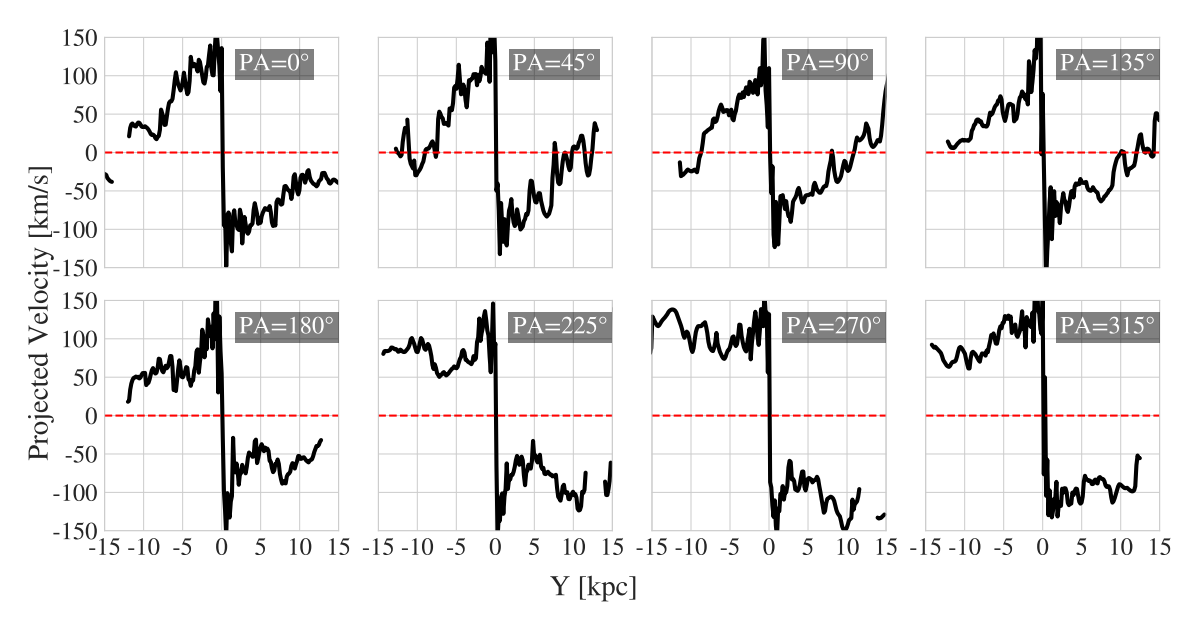


Figure 10. Corresponding Position-Velocity plots for the ideal first moment maps shown in Fig. 9. Velocities are taken from the disk minor axis. Velocity inversions caused by the warp can be seen in  $PA = 45^{\circ}-135^{\circ}$ . The rotation curves appear much flatter in  $PA = 225^{\circ}-315^{\circ}$ , despite being strongly centrally peaked.

nor axis (e.g., PA=0°, 180°), there are noticeable deviations from rotation. When the warp is anti-aligned with the observed disk major axis (PA=90°), a velocity inversion is present, where the sign of the projected velocity switches near the disk edge. Such velocity inversions can be observed in H I observations of galaxies (X. Lin et al. 2025; J. Healy et al. 2024) and will be discussed further in Sec. 7.2. This is further visualized in Fig. 10, which shows the corresponding Position-Velocity diagrams for these plots. Velocities were taken from the central pixel

along a vertical line in each orientation, to fully characterize the rotation curve of the inner disk. Notably, when the warp axis is perfectly aligned with the observed disk major axis (PA=270°), the rotation curve appears relatively flat despite having a strong central peak.

# 7. DISCUSSION OF IMPLICATIONS FOR OBSERVATIONS

While the FOGGIE simulations broadly agree with the observed H I Size-Mass relation, the details of how

much H I there exists outside the inner disk, as well as the observable orientation and dynamics of the H I in the extended disk, depend heavily on the observational parameters and observed viewing angle. In order to interpret observations properly and make robust comparisons to simulations, these effects must be taken into account. In the following subsections we will discuss the feasibility of observing the extended H I emission outside of the disk in real galaxies (Sec. 7.1), how to compare between simulations and observations (Sec. 7.2), and numerical resolution effects important in this study (Sec. 7.3).

## 7.1. How to observe extended H I emission

Detecting low column density gas in the CGM has been a longstanding problem of interest in astronomy. Historically, the detection of this gas was largely constrained to absorption studies (e.g., H.-W. Chen 2012; N. M. Nielsen et al. 2013; J. K. Werk et al. 2014; S. Borthakur et al. 2015; G. G. Kacprzak et al. 2015; M. A. Berg et al. 2019; C. Péroux et al. 2019; F. S. Zahedy et al. 2019; N. Lehner et al. 2025), as column densities were too low to be observed in emission. Simulation studies have predicted a variety of morphologies, and often show sharp drop-offs in H I column density at the disk edge (e.g., M. Mina et al. 2021; C. W. Trapp et al. 2022; R. Ramesh et al. 2023; D. R. Piacitelli et al. 2025). Many of these simulation suites focus their resolution elements on high-density regions, which preferentially targets the inner star-forming disk. The simulations presented here instead focus computational power on better resolving the material in the CGM, allowing for increasingly complex structures to emerge that are not seen in other suites. This further complicates the picture, as it allows for both spatially diffuse and spatially compact structures to be resolved within the CGM of our simulations (see FOGGIE XII for more details). To fully characterize the H I outside the disk, studies must be sensitive to both of these spatial scales.

Even with only the six galaxies presented here, we see a large variance in the amount of detectable CGM material in different interferometry studies (Fig. 2, 3). In systems like Tempest, for instance, small spatial scale, clumpy material dominates the CGM. This material is almost entirely missing from observations due to sensitivity and resolution effects for most instruments, and the effects of missing short baselines are largely negligible. Systems like Blizzard or Hurricane, however, show much more diffuse signal. While signal is still lost to resolution effects, much is also lost due to the missing short baseline problem. Furthermore, the effects of this spatial filtering can be highly dependent on the observed

viewing angle of the system in combination with its morphology. This makes the formulation of a simple correction to account for this missing signal impossible, or at the very least, subject to large uncertainties. While a loss of up to 40% of observable CGM H I due to interferometric effects may seem acceptable, it is important to keep in mind that this effect is strongly biased towards missing diffuse components of gas. As it is currently unclear how much of the actual baryon content in the CGMs of real galaxies is in the diffuse component versus clumpy structures (and likely varies strongly), it is impossible to know how much we may be missing from a given observation.

The next generation of interferometers will go a long way to alleviating this problem. As seen in Table 2, the enhanced spatial resolution and sensitivity an instrument similar to the Square Kilometer Array (SKA) will provide will allow for much more of this material to be detected. Even Tempest, however, still suffers from the missing short baseline problem in this case. Further development of deconvolutional algorithms is unlikely to improve this, as the low spatial frequency is fundamentally missing from these observations. Instead, these spatial frequencies must be sampled somehow. As seen in Fig. 7, depending on the system, baselines of a few meters must be sampled to observe over 90\% of the CGM H I signal. This likely requires the combination of data from large single-dish radio telescopes with interferometers in order to more fully sample the UV plane. A few studies utilizing data from the Five-hundred-meter Aperture Spherical radio Telescope (FAST) (J. Wang et al. 2024) as well as the Green Bank Telescope (GBT) (C. Eibensteiner et al. 2023; E. W. Koch et al. 2025) have already experimented with this. The combination of large single dishes with high-sensitivity interferometry surveys such as MHONGOOSE (W. J. G. de Blok et al. 2024) and future surveys with the SKA will be of particular interest.

# 7.2. On comparisons between observation and simulation

As instruments become able to probe deeper H I column densities and cosmological simulations continue to advance in both resolution and complexity of physics, robust comparisons between the two are vital for both validating simulations as well as understanding and interpreting observations. We highlight two broad effects in this study. The first is the importance of robust forward modeling of simulation data to synthetic image data. As emphasized in Fig. 5, the consideration of missing short baselines dramatically alters the observed distribution of gas. With this consideration, the three Less

Populated systems in our sample track recent observations much more closely (A. Marasco et al. 2025). The importance of robust forward modeling applies to many different topics in astrophysics, including HI-based rotation curves (e.g., A. V. Macciò et al. 2016; A. M. Brooks et al. 2017; D. Ruan et al. 2025), metallicity gradients (e.g., Z. S. Hemler et al. 2021; A. Acharyya et al. 2025; R. L. Graf et al. 2024), simulation-based inference (e.g., C. Hahn et al. 2022), and more.

A second important effect is the significant and nonintuitive effects that the viewing angle has on these systems. The effect of inclination and the observed position of the disk relative to the major axis is well known on measured kinematics. As shown in Fig. 8, both the observed inclination and position angle of a warped system can have significant effects on the observable amount of CGM material. Similarly, as shown in Fig. 9 and Fig. 10, the observed position angle of a warped system can have dramatic effects on the observed kinematics, leading to velocity inversions in one orientation and incorrectly measured flat rotation curves in the opposite orientation. If models that are fit to similar galaxies cannot reliably fit these types of inclination warps, or if we do not have a characteristic signature to know a warp is present, the fits for both rotational and radial velocities may be compromised.

As H I 21-cm observations probe deeper column densities, it should be expected that more signatures of these warps may be found. For instance, J. Healy et al. (2024) shows evidence of a warp in the extended H I disk of NGC 5068 in the MHONGOOSE survey, with the outer regions of the first moment map twisted in an S-shape. The pattern of this velocity field is strikingly similar to the velocity field seen in Tempest at a position angle of 45°, as seen in the second panel of Fig. 8. If this warp was rotated in some other orientation with respect to the inclination axis, this signature would not be so easy to point out in a simple moment map, and would require advanced modeling techniques to recover.

Similarly, X. Lin et al. (2025) shows a stark velocity inversion between the inner disk and extended, diffuse H I of M51 in the FEASTS survey. Importantly, FEASTS utilizes dual convolutions with interferometric data from the VLA (F. Walter et al. 2008) and single dish data from the FAST telescope, however, they do not explicitly claim a warped structure in the extended disk. The velocity field signature is reminiscent of what is seen in Tempest at a position angle of 90° (Fig. 8), however, to a much larger extent. This implies that there is a large warp in the extended, diffuse material of M51, likely related to interactions with the nearby dwarf galaxy. Again, we note that this velocity inversion re-

quires a specific orientation on the sky with respect to the warp. Given the size of the M51's extended disk, it is more likely to be observed than more modest warps.

## 7.3. On Spatial Resolution

Important to the consideration of H I in extended disks is the numerical spatial resolution of the simulations and how it compares to both the spatial resolution of observations as well as the maximum observable scale of an interferometer. The FOGGIE simulations are particularly well suited to this type of study, as their spatial resolution at redshift z=0 ( $\Delta x=0.274$  kpc) is of similar resolution to current interferometers (i.e.  $\sim 0.262$ kpc for MeerKAT at 10 Mpc). Additionally, the forced resolution in the CGM ( $\Delta x = 1.10 \text{ kpc}$ ) is much smaller than the maximum observable scale ( $\sim 60 \text{ kpc}$  for the 21cm line at 10 Mpc). For simulations that do not enforce a fixed spatial resolution in the CGM, caution must be taken when drawing comparisons. If the scale of the resolution element is close to this maximum observable scale, the CGM will not be visible when spatially filtered due to purely numerical resolution effects.

As discussed previously, the H I emission that is lost due to the missing short baseline problem tends to come from low column density material outside the disk, meaning it may be difficult for classical zoom-in simulations to resolve. Of interest is the mass resolution of the cells in our simulations that end up being filtered out in the spatial filtering step. In this study, the H I weighted average cell mass of these cells is  $\sim 10^3~M_{\odot}$ . This is well below the mass resolution of other state-of-the-art simulations ( $\sim 10^4~M_{\odot}$ ), implying that FOGGIE is better situated to resolve this missing material. For a more detailed discussion of resolution in the FOGGIE disks and CGM, see Appendix A of FOGGIE XII.

## 8. SUMMARY

This is the second part of a two-paper series in which we investigate the evolution and observable properties of the extended H I disks in Milky Way-mass galaxies using zoom-in simulations from the Figuring Out Gas & Galaxies in Enzo (FOGGIE) simulation suite. FOG-GIE XII focuses on the origin and properties of the extended and misaligned H I disks in these systems. This paper focused on the observable properties of these systems, how they would appear in interferometric radio observations, and how projection effects may alter observed properties. We categorize systems into those with Less Populated and More Populated CGMs following FOGGIE XII. Less Populated systems form thin disks and have hot inner CGMs near their virial temperature. while More Populated systems do not. Our conclusions are as follows.

- The H I Size-Mass relation for all but one system falls within the  $3\sigma$  scatter from observations. Cyclone is slightly overmassive for its size, likely due to recent satellite interactions leading to a compact disk.
- To match interferometric studies, we spatially filter our smoothed, synthetic H I 21-cm datacubes to remove spatially diffuse signal. The overall measured flux is largely unaffected by this. The CGM of the Less Populated systems with only small-scale clumpy emission is also largely unaffected. The CGM of More Populated systems, with more diffuse emission, lose up to 10–40% of their observable signal.
- These systems show an over-abundance of low column density  $(N_{HI} < 10^{20} \text{ cm}^{-2})$  gas when compared with recent interferometric studies. Spatially filtering these images to remove diffuse signal and mimic the effects of missing short baselines preferentially removes the low column density, low velocity dispersion gas. This brings our simulations into better agreement with recent observations.
- To fully capture the emission from these extended and diffuse H I structures, dual convolutions with single dish instruments are needed (e.g., C. Eibensteiner et al. 2023; J. Wang et al. 2025; E. W. Koch et al. 2025)
- Observed inclination can alter the amount of detectable material to interferometric studies (~ 10% based on changing the galaxy's spatial scale on the sky). If significant misaligned gas is present, the observed position angle can have significant effects as well.
- Viewing a warped system at different position angles can lead to observed velocity inversions or flat rotation curves not present in the actual data.

As we are able to probe deeper and deeper column densities of H I in and around galaxies, we stand to gain new insights into how galaxies grow, evolve, and sustain their star formation. If the diffuse component of the H I emission signal is as prevalent (or more) than what we see in our simulations, current and future interferometry studies may be missing out on a key component of this extended emission. Other simulations may also be missing this same material if their CGM resolution is coarser than what FOGGIE can achieve. In order to constrain this missing component, as well as test and validate simulations, dual convolutions with large single-dish data

are required. This, as well as the ability to model complex dynamics of such systems, is highly dependent on the observed viewing angle, implying that simulations will play an important role in interpreting current and future observation and may also need to increase their resolving power to fully track the cycle of baryons in and out of galaxies.

## ACKNOWLEDGMENTS

We thank N. Lehner for helpful comments and sug-CT was supported for this work in part by NASA via a Theoretical and Computational Astrophysics Networks grant #80 NSSC 21 K 1053 and JWST AR #5486. VS was supported for this work in part by NASA via an Astrophysics Theory Program grant #80NSSC24K0772, HST AR #17549, and HST GO CT and VS were additionally supported #17093.by HST AR #16151. BWO acknowledges support from NSF grants #1908109 and #2106575, NASA ATP grants 80NSSC18K1105 and 80NSSC24K0772, and NASA TCAN grant 80NSSC21K1053. AA acknowledges support from the INAF Large Grant 2022 Extragalactic Surveys with JWST (PI Pentericci) and from the European Union NextGenerationEU RFF M4C2 1.1 PRIN 2022 project 2022ZSL4BL INSIGHT. RA acknowledges funding from the European Research Council (ERC) under the European Union's Horizon 2020 research and innovation programme (grant agreement 101020943, SPECMAP-CGM).

Computations described in this work were performed using the publicly-available ENZO code (http://enzo-project.org), which is the product of a collaborative effort of many independent scientists from numerous institutions around the world. Their commitment to open science has helped make this work possible. The software package SOFIA-2 (T. Westmeier et al. 2021) was used to extract sources from synthetic images. The python packages MATPLOTLIB (J. D. Hunter 2007), NUMPY (S. v. d. Walt et al. 2011), ROCKSTAR (P. S. Behroozi et al. 2013), TANGOS (A. Pontzen & M. Tremmel 2018), SCIPY (P. Virtanen et al. 2020), YT (M. J. Turk et al. 2011), and ASTROPY (Astropy Collaboration et al. 2013, 2018, 2022) were all used in parts of this analysis or in products used by this paper.

Resources supporting this work were provided by the NASA High-End Computing (HEC) Program through the NASA Advanced Supercomputing (NAS) Division at Ames Research Center and were sponsored by NASA's Science Mission Directorate; we are grateful for the superb user-support provided by NAS. Computations described in this work were performed using the

publicly-available Enzo code, which is the product of a collaborative effort of many independent scientists from numerous institutions around the world.

### AUTHOR CONTRIBUTIONS

CT led the analysis and writing of the paper. MSP, BWO, and JT are the principal investigators of the FOGGIE collaboration; they obtained funding for, developed, ran the simulations used in this work, and provided valuable feedback and insights throughout the project. ACW characterized satellite evolution and pro-

vided feedback on the draft. BDS contributed through discussions and feedback on the draft and developed the initial conditions for the FOGGIE simulations. AA provided insight into synthetic image generation and feedback on the draft. VS assisted in figure design and provided feedback on the draft. RA contributed through discussions during the analysis phase and feedback on the draft.

### REFERENCES

- Acharyya, A., Peeples, M. S., Tumlinson, J., et al. 2025, ApJ, 979, 129, doi: 10.3847/1538-4357/ad9dd8
- Astropy Collaboration, Robitaille, T. P., Tollerud, E. J., et al. 2013, A&A, 558, A33,
  - doi: 10.1051/0004-6361/201322068
- Astropy Collaboration, Price-Whelan, A. M., Sipőcz, B. M., et al. 2018, AJ, 156, 123, doi: 10.3847/1538-3881/aabc4f
- Astropy Collaboration, Price-Whelan, A. M., Lim, P. L., et al. 2022, ApJ, 935, 167, doi: 10.3847/1538-4357/ac7c74
- Behroozi, P. S., Wechsler, R. H., & Wu, H.-Y. 2013, ApJ, 762, 109, doi: 10.1088/0004-637X/762/2/109
- Berg, M. A., Howk, J. C., Lehner, N., et al. 2019, ApJ, 883, 5, doi: 10.3847/1538-4357/ab378e
- Blue Bird, J., Davis, J., Luber, N., et al. 2020, MNRAS, 492, 153, doi: 10.1093/mnras/stz3357
- Borthakur, S., Heckman, T., Tumlinson, J., et al. 2015, ApJ, 813, 46, doi: 10.1088/0004-637X/813/1/46
- Broeils, A. H., & Rhee, M. H. 1997a, A&A, 324, 877
- Broeils, A. H., & Rhee, M. H. 1997b, A&A, 324, 877
- Brooks, A. M., Papastergis, E., Christensen, C. R., et al. 2017, ApJ, 850, 97, doi: 10.3847/1538-4357/aa9576
- Brummel-Smith, C., Bryan, G., Butsky, I., et al. 2019, The Journal of Open Source Software, 4, 1636, doi: 10.21105/joss.01636
- Bryan, G. L., Norman, M. L., O'Shea, B. W., et al. 2014, ApJS, 211, 19, doi: 10.1088/0067-0049/211/2/19
- Chen, H.-W. 2012, MNRAS, 427, 1238, doi: 10.1111/j.1365-2966.2012.22053.x
- Corlies, L., Peeples, M. S., Tumlinson, J., et al. 2020, ApJ, 896, 125, doi: 10.3847/1538-4357/ab9310
- de Blok, W. J. G., Keating, K. M., Pisano, D. J., et al. 2014, A&A, 569, A68, doi: 10.1051/0004-6361/201423880
- de Blok, W. J. G., Healy, J., Maccagni, F. M., et al. 2024, Astronomy & Astrophysics, 688, A109, doi: 10.1051/0004-6361/202348297

- Eibensteiner, C., Bigiel, F., Leroy, A. K., et al. 2023, A&A, 675, A37, doi: 10.1051/0004-6361/202245290
- Fraternali, F., van Moorsel, G., Sancisi, R., & Oosterloo, T. 2002, AJ, 123, 3124, doi: 10.1086/340358
- Graf, R. L., Wetzel, A., Bailin, J., & Orr, M. E. 2024, arXiv e-prints, arXiv:2410.21377,
  - doi: 10.48550/arXiv.2410.21377
- Hahn, C., Eickenberg, M., Ho, S., et al. 2022, arXiv e-prints, arXiv:2211.00723,
  - doi: 10.48550/arXiv.2211.00723
- Heald, G., Józsa, G., Serra, P., et al. 2011, A&A, 526, A118, doi: 10.1051/0004-6361/201015938
- Healy, J., de Blok, W. J. G., Maccagni, F. M., et al. 2024, Astronomy & Astrophysics, 687, A254, doi: 10.1051/0004-6361/202347475
- Hemler, Z. S., Torrey, P., Qi, J., et al. 2021, MNRAS, 506, 3024, doi: 10.1093/mnras/stab1803
- Högbom, J. A. 1974, A&AS, 15, 417
- Hunter, J. D. 2007, Computing in Science and Engineering, 9, 90, doi: 10.1109/MCSE.2007.55
- Jiao, Q., Zhu, M., Vollmer, B., et al. 2025, ApJ, 986, 46, doi: 10.3847/1538-4357/add0ba
- Kacprzak, G. G., Muzahid, S., Churchill, C. W., Nielsen, N. M., & Charlton, J. C. 2015, ApJ, 815, 22, doi: 10.1088/0004-637X/815/1/22
- Kennicutt, Jr., R. C. 1998, ApJ, 498, 541, doi: 10.1086/305588
- Koch, E. W., Leroy, A. K., Rosolowsky, E. W., et al. 2025, ApJS, 279, 35, doi: 10.3847/1538-4365/ade0ad
- Lehner, N., Kopenhafer, C., O'Meara, J. M., et al. 2022, ApJ, 936, 156, doi: 10.3847/1538-4357/ac7400
- Lehner, N., Howk, J. C., Collins, L., et al. 2025, arXiv e-prints, arXiv:2506.16573,
  - doi: 10.48550/arXiv.2506.16573
- Lin, X., Wang, J., Staveley-Smith, L., et al. 2025, ApJ, 982, 151, doi: 10.3847/1538-4357/adb718

- Lochhaas, C., Peeples, M. S., O'Shea, B. W., et al. 2025, arXiv e-prints, arXiv:2510.25844. https://arxiv.org/abs/2510.25844
- Macciò, A. V., Udrescu, S. M., Dutton, A. A., et al. 2016, MNRAS, 463, L69, doi: 10.1093/mnrasl/slw147
- Marasco, A., de Blok, W. J. G., Maccagni, F. M., et al. 2025, Astronomy & Astrophysics, 697, A86, doi: 10.1051/0004-6361/202453172
- McGaugh, S. S., Schombert, J. M., Bothun, G. D., & de Blok, W. J. G. 2000, ApJL, 533, L99, doi: 10.1086/312628
- Mina, M., Shen, S., Keller, B. W., et al. 2021, A&A, 655, A22, doi: 10.1051/0004-6361/202039420
- Nielsen, N. M., Churchill, C. W., & Kacprzak, G. G. 2013, ApJ, 776, 115, doi: 10.1088/0004-637X/776/2/115
- Peeples, M. S., Corlies, L., Tumlinson, J., et al. 2019, ApJ, 873, 129, doi: 10.3847/1538-4357/ab0654
- Péroux, C., Zwaan, M. A., Klitsch, A., et al. 2019, MNRAS, 485, 1595, doi: 10.1093/mnras/stz202
- Piacitelli, D. R., Brooks, A. M., Christensen, C., et al. 2025, arXiv e-prints, arXiv:2505.08861, doi: 10.48550/arXiv.2505.08861
- Pisano, D. J. 2014, AJ, 147, 48, doi: 10.1088/0004-6256/147/3/48
- Pontzen, A., & Tremmel, M. 2018, ApJS, 237, 23, doi: 10.3847/1538-4365/aac832
- Ramesh, R., Nelson, D., & Pillepich, A. 2023, MNRAS, 518, 5754, doi: 10.1093/mnras/stac3524
- Ruan, D., Brooks, A. M., Cruz, A., et al. 2025, MNRAS, 541, 2180, doi: 10.1093/mnras/staf1099
- Saintonge, A., Tacconi, L. J., Fabello, S., et al. 2012, ApJ, 758, 73, doi: 10.1088/0004-637X/758/2/73
- Simons, R. C., Peeples, M. S., Tumlinson, J., et al. 2020, ApJ, 905, 167, doi: 10.3847/1538-4357/abc5b8
- Thilker, D. A., Braun, R., Walterbos, R. A. M., et al. 2004, ApJL, 601, L39, doi: 10.1086/381703

- Trapp, C., Peeples, M. S., Tumlinson, J., & et al. 2025, ApJ. https://arxiv.org/abs/2510.tbd
- Trapp, C. W., Kereš, D., Chan, T. K., et al. 2022, MNRAS, 509, 4149, doi: 10.1093/mnras/stab3251
- Tully, R. B., & Fisher, J. R. 1977, A&A, 54, 661
- Turk, M. J., Smith, B. D., Oishi, J. S., et al. 2011, The Astrophysical Journal Supplement Series, 192, 9, doi: 10.1088/0067-0049/192/1/9
- Veronese, S., de Blok, W. J. G., Healy, J., et al. 2025, A&A, 693, A97, doi: 10.1051/0004-6361/202452085
- Virtanen, P., Gommers, R., Oliphant, T. E., et al. 2020, Nature Methods, 17, 261, doi: 10.1038/s41592-019-0686-2
- Walt, S. v. d., Colbert, S. C., & Varoquaux, G. 2011, Computing in Science & Engineering, 13, 22
- Walter, F., Brinks, E., de Blok, W. J. G., et al. 2008, The Astronomical Journal, 136, 25632647, doi: 10.1088/0004-6256/136/6/2563
- Wang, J., Koribalski, B. S., Serra, P., et al. 2016, MNRAS, 460, 2143, doi: 10.1093/mnras/stw1099
- Wang, J., Lin, X., Yang, D., et al. 2024, ApJ, 968, 48, doi: 10.3847/1538-4357/ad3e61
- Wang, J., Yang, D., Lin, X., et al. 2025, ApJ, 980, 25, doi: 10.3847/1538-4357/ada95a
- Werk, J. K., Prochaska, J. X., Tumlinson, J., et al. 2014, ApJ, 792, 8, doi: 10.1088/0004-637X/792/1/8
- Westmeier, T., Kitaeff, S., Pallot, D., et al. 2021, MNRAS, 506, 3962, doi: 10.1093/mnras/stab1881
- Wright, A. C., Tumlinson, J., Peeples, M. S., et al. 2024, ApJ, 970, 70, doi: 10.3847/1538-4357/ad49a3
- Zahedy, F. S., Chen, H.-W., Johnson, S. D., et al. 2019, MNRAS, 484, 2257, doi: 10.1093/mnras/sty3482
- Zheng, Y., Peeples, M. S., O'Shea, B. W., et al. 2020, ApJ, 896, 143, doi: 10.3847/1538-4357/ab960a
- Zwaan, M. A., Briggs, F. H., Sprayberry, D., & Sorar, E. 1997, ApJ, 490, 173, doi: 10.1086/304872